Quality Control of Bump-bonded Detector Modules for the CMS Pixel Upgrade

James Cameron, DESY

September 5, 2014

Abstract

Owing to the proposal of a luminosity increase of the Large Hadron Collider, the Compact Muon Solenoid pixel detector is due to receive an upgrade in 2016/2017. There currently exists no simple method of quality control for the new pixel modules being constructed by the Paul Scherrer Institute and the Deutsches Elektronen-Synchrotron. The modules are hybrid pixel detectors in that the Read-Out Chips are flip-chip bump-bonded to the silicon sensor. Laid out in this report are two related methods of determining the height variation over the Read-Out Chips on the modules in a simple and non-destructive manner. The methods exploit the variation of the capacitance between the sensor and the Read-Out Chip caused by the height variation of the bump-bond connections. The accuracy of the techniques is supported by comparisons to direct height measurements laboriously obtained using the variable focal length of a microscope. The two methods are consistent with each other, and both produce a quantitative measure of the height variation. It is determined that a test pulse threshold ratio gradient of 0.25 delivered by either method corresponds to a height variation of 6 μm over the ROC.

Contents

1 Introduction

The Compact Muon Solenoid (CMS) detector is one of the large, general-purpose experiments conducted on the Large Hadron Collider (LHC) at the European Organisation for Nuclear Research (CERN), based in Geneva[1]. The primary aims of the CMS experiment are to explore high energy physics at the TeV scale, study the properties of the Higgs boson, study heavy ion collisions, and to search for evidence of physics beyond the standard model, such as supersymmetry[2]. The CMS detector is built around the eponymous solenoidal magnet, which constitutes the bulk of the detector, and is capable of producing a magnetic field of 3.8 T. The detector has a layered structure; the outermost layer is devoted to detecting muons, and going inwards, the next layers are the hadronic and electromagnetic calorimeters, intended to detect hadronic and electromagnetic energy, and finally, in the innermost layer at the heart of the detector, is the silicon-based tracker. The High Luminosity LHC (HL-LHC) is a proposed upgrade to the current LHC, and aims to increase the luminosity by a factor of up to 5[3]. This increase would cause the efficiency of the CMS detector to suffer, and as such, an upgrade to the CMS pixel detector due in 2016/2017 is also proposed, the specifications of which are designed to reduce the mass of the detector, increase its efficiency, and minimise its radiation degradation[4].

The upgraded pixel detector will be comprised of approximately 1200 hybrid pixel modules in the barrel, each with 66,560 individual 100 μm $\times$ 150 μm silicon pixels divided between 16 Read-Out Chips (ROCs), for a total of approximately 80 million pixels[4]. Hybrid pixel module means that the solid-state sensor is bump- or wire-bonded to CMOS ROCs. The pixels on each ROC are arranged in 52 columns and 80 rows. The ROCs are bump-bonded to the silicon sensor, which is glued to the module's High Density Interconnect (HDI). The sensor is wire-bonded to the HDI in one corner for the bias voltage, required for producing the depletion layer, and the ROCs are wire-bonded to the long edges of the HDI. The read-out of the signals is facilitated by a Token Bit Manager (TBM), glued and wire-bonded to the module, which allows the signal from each ROC to be transmitted via a shared data line. The construction of one such module is depicted in Figure 1.

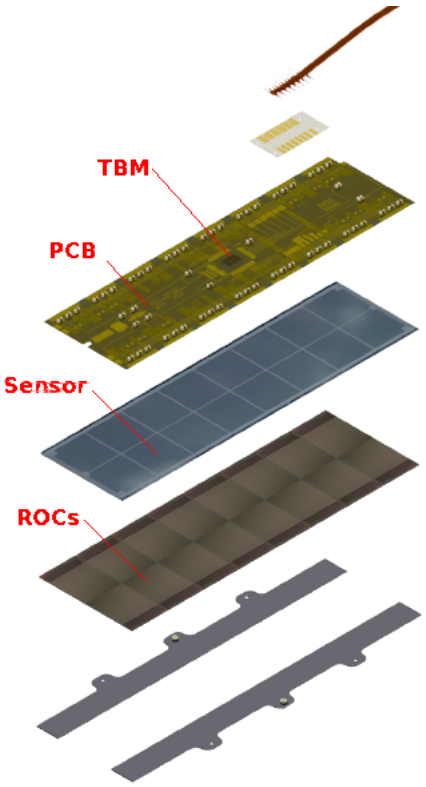

Figure 1: An exploded diagram of a module, showing the HDI, the silicon sensor, and the ROCs.

A charged particle passing through the depletion region creates electron-hole pairs along its track. The strong electric field over the region causes the holes to drift away from the amplifiers, and the electrons to drift towards them. The electrons are collected, registering a negative charge which is passed to a preamplifier and a shaper, compared to a threshold via a comparator, and if appropriate, stored, ready to be read out.

Nominally, the height of a bump-bond post reflow is 25 μm, but it is subject to systematic variation caused by the assembly procedure. While testing the electrical properties of the bump-bonds is trivial, there currently exists no simple, quick, or non-destructive method to measure the variation in height, and in this report, a proposal is made for an effective method of determining the height variation over a ROC, which could provide a rudimentary form of quality control for the in-house bump-bonding process.

2 Theory

There exists two ways of applying a test pulse to the ROC; directly through C_{cal}, (VCal method), or via the bump-bond and C_{air}, (Cals method), formed by metal pads on the sensor and the ROC. The pulse heights, PH, measured for each of these is proportional to the charge registered, Q,

$$PH_{VCal} = g \cdot Q_{VCal} = g \cdot C_{cal} \cdot VCal \tag{1}$$

$$PH_{Cals} = g \cdot Q_{Cals} = g \cdot C_{air} \cdot VCal \tag{2}$$

where g is the gain of the amplifier, and $VCal$ is the amplitude of the test pulse. Taking the ratio of the pulse heights gives a ratio of the capacitance values, and using the equation for a parallel plate capacitor $C = \epsilon \cdot \frac{A}{d}$,

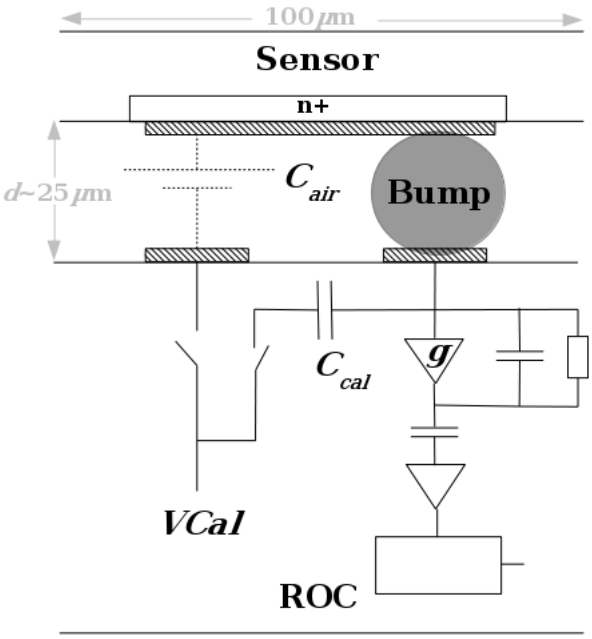

Figure 2: The circuitry involved in applying a test pulse. VCal method: Test pulse via C_{cal} to the amplifier. Cals method: Test pulse via C_{air} and the bump-bond to the preamplifier.

$$\frac{PH_{VCal}}{PH_{Cals}} = \frac{C_{cal}}{C_{air}} = \frac{C_{cal}}{\epsilon \cdot A} \cdot d \propto d \tag{3}$$

where ϵ is the permittivity, A is the area of the metal plates, and d is the height of the bump-bond. Here, d is the only non-constant parameter, so the ratio of the pulse heights is directly proportional to the height of the bump-bond.

The preamplifier is charge sensitive, and at the comparator both test pulses encounter the same threshold in charge units. The threshold, Thr, in charge units of each pulse is

$$Thr_{VCal} = g \cdot C_{cal} \cdot VCal_{thrVCal} \tag{4}$$

$$Thr_{Cals} = g \cdot C_{air} \cdot VCal_{thrCals} \tag{5}$$

where $VCal_{thr}$ is the threshold in $VCal$ units. The thresholds are equal in charge units, but due to different capacitances, the thresholds for the two pulses appear at different values in $VCal$ units. Equating the charge thresholds, cancelling the gain, and rearranging gives

$$\frac{C_{cal}}{C_{air}} = \frac{VCal_{thrCals}}{VCal_{thrVCal}} \propto d \tag{6}$$

Therefore, by producing so called "S-Curves" by scanning $VCal$ and recording the number of responses for each of the test pulses, the thresholds in $VCal$ units can be measured. By performing this action for each of the 4160 pixels on a ROC, the variation in height over the ROC can be observed.

In a similar way, the noise, which is manifested in the width of the S-Curves, is equal in charge units for each test pulse because it is an intrinsic property of the preamplifier, but it has different values in $VCal$ units due to the different capacitances. This can also be exploited to examine the trend in height over the ROC.

3 Measurements

The S-Curves of an arbitrarily chosen pixel are shown in Figure 3.

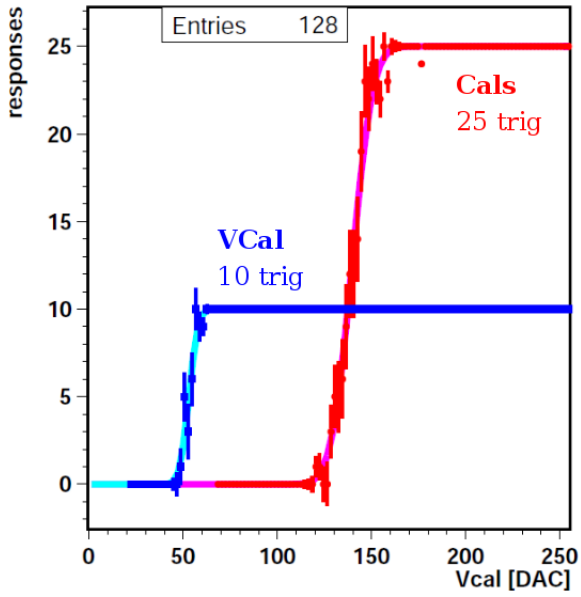

Figure 3: S-Curves of pixel 1793, ROC 15, module D4009. In blue is the $VCal$ test pulse performed with 10 triggers, and in red the $Cals$ test pulse with 25 triggers. The curves are produced by fitting a Gaussian error function.

The thresholds in $VCal$ units are taken as the point at which the number of responses is 50% of the number of triggers. From the S-Curves of each pixel, the threshold and width of the $VCal$ and $Cals$ test pulses can be extracted and their ratios plotted in a pixel map for the ROC.

Modules D4003, D4004, D4005, and D4006 have had the height variation over each of their ROCs directly measured by means of measuring the difference between the distance required to focus a microscope on the back of the sensor and the distance required to focus on the top of each corner of the ROCs. The variation over a single ROC is typically in the region of 2 μm - 8 μm, and the ROCs have a tendency to be lower at the edges of the module and higher along the centre line forming a roof-like structure, indicating that during the mounting process more pressure is applied towards the edges.

3.1 Threshold Ratio Maps

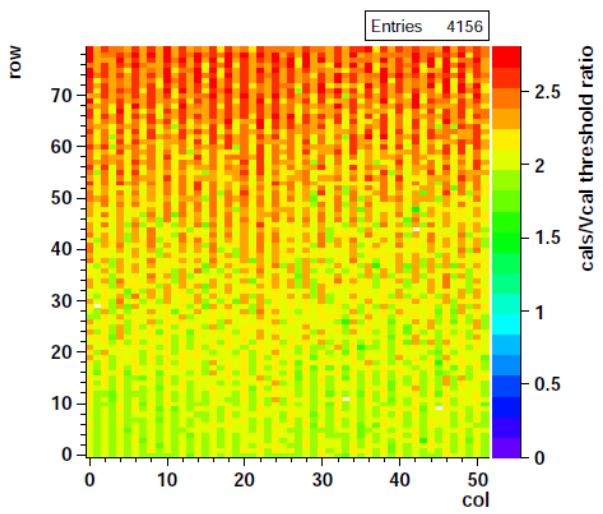

(a) ROC 03, module D4003. There are 4 missing entries.

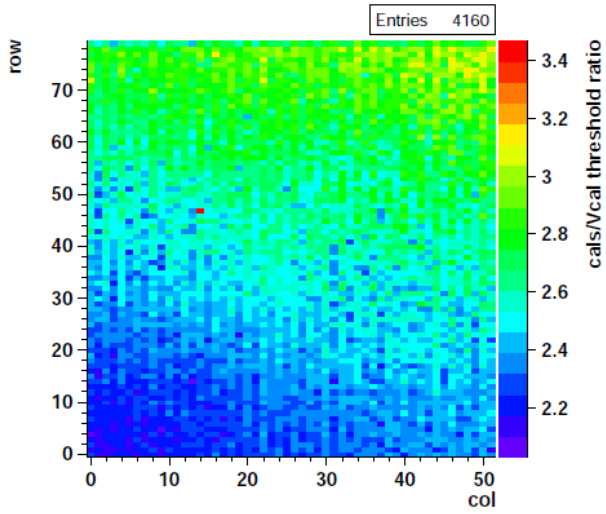

(b) ROC 06, module D4004. There is 1 anomalous pixel in the trend.

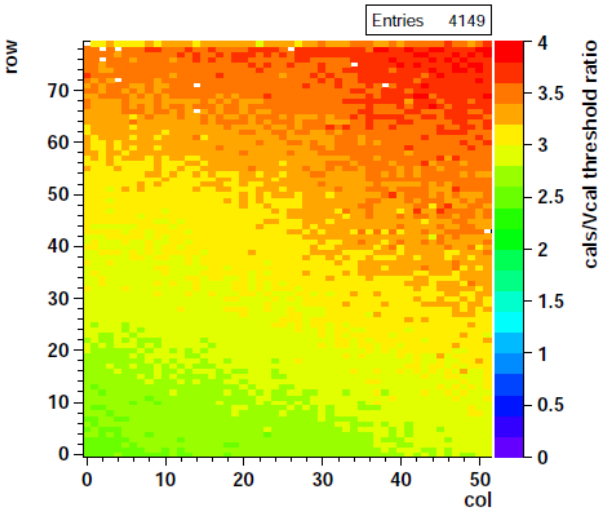

(c) ROC 07, module D4005. There are 11 missing entries.

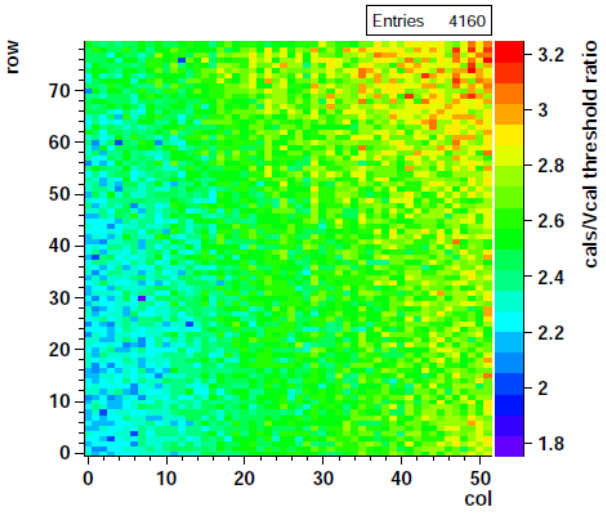

(d) ROC 15, module D4006.

Figure 4: A threshold ratio map of a ROC from each of the modules that have had their bump-bond heights directly measured. Higher threshold ratio should indicate a taller bump-bond.

Figure 4 shows a threshold ratio map from a ROC from each of the modules which have had their height variation measured with the microscope. The majority of the 62 maps (ROC 09, module D4003, and ROC 01, module D4006 are dead) produced exhibit a trend in the row direction, confirming the "house roof" assertion. Far fewer of the ROCs exhibit a trend in the column direction, such as in Figures 4(b), 4(c), and 4(d), and the trends in the column direction are also generally much weaker than those in the row direction. On many of the ROCs there also exists a peculiar even/odd effect in the column direction, which is nicely demonstrated in Figure 4(a), and this observation remains unexplained.

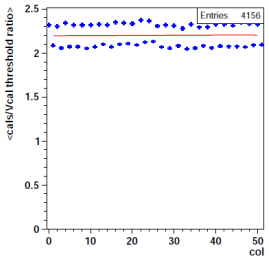

(a) ROC 03, module D4003 columns.

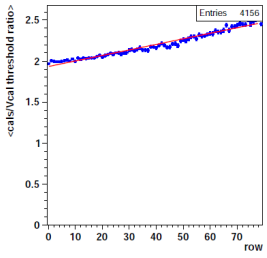

(b) ROC 03, module D4003 rows.

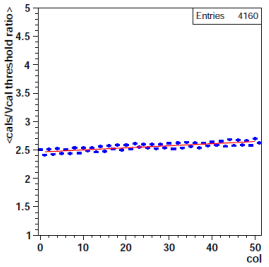

(c) ROC 06, module D4004 columns.

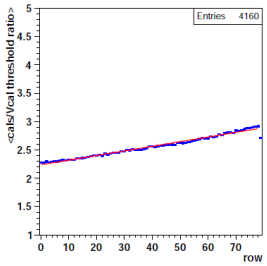

(d) ROC 06, module D4004 rows.

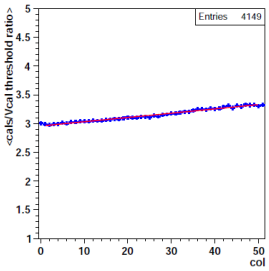

(e) ROC 07, module D4005 columns.

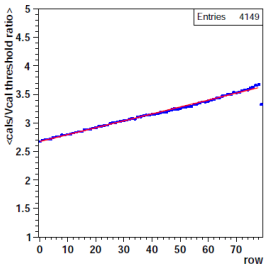

(f) ROC 07, module D4005 rows.

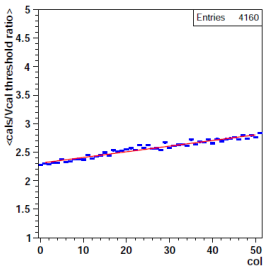

(g) ROC 15, module D4006 columns.

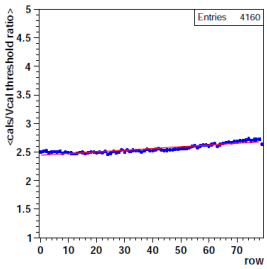

(h) ROC 15, module D4006 rows.

Figure 5: Column and row threshold ratio projections from the threshold ratio maps.

Figure 5 shows separate column and row projections of the threshold ratio maps. The even/odd effect is again clearly visible on some of the column projections. Most of the modules tested exhibit a positive gradient in the row direction, forming the roof like structure. In Figure 6, the gradients of these column and row projections are plotted against direct measurements of the height variation obtained with the microscope.

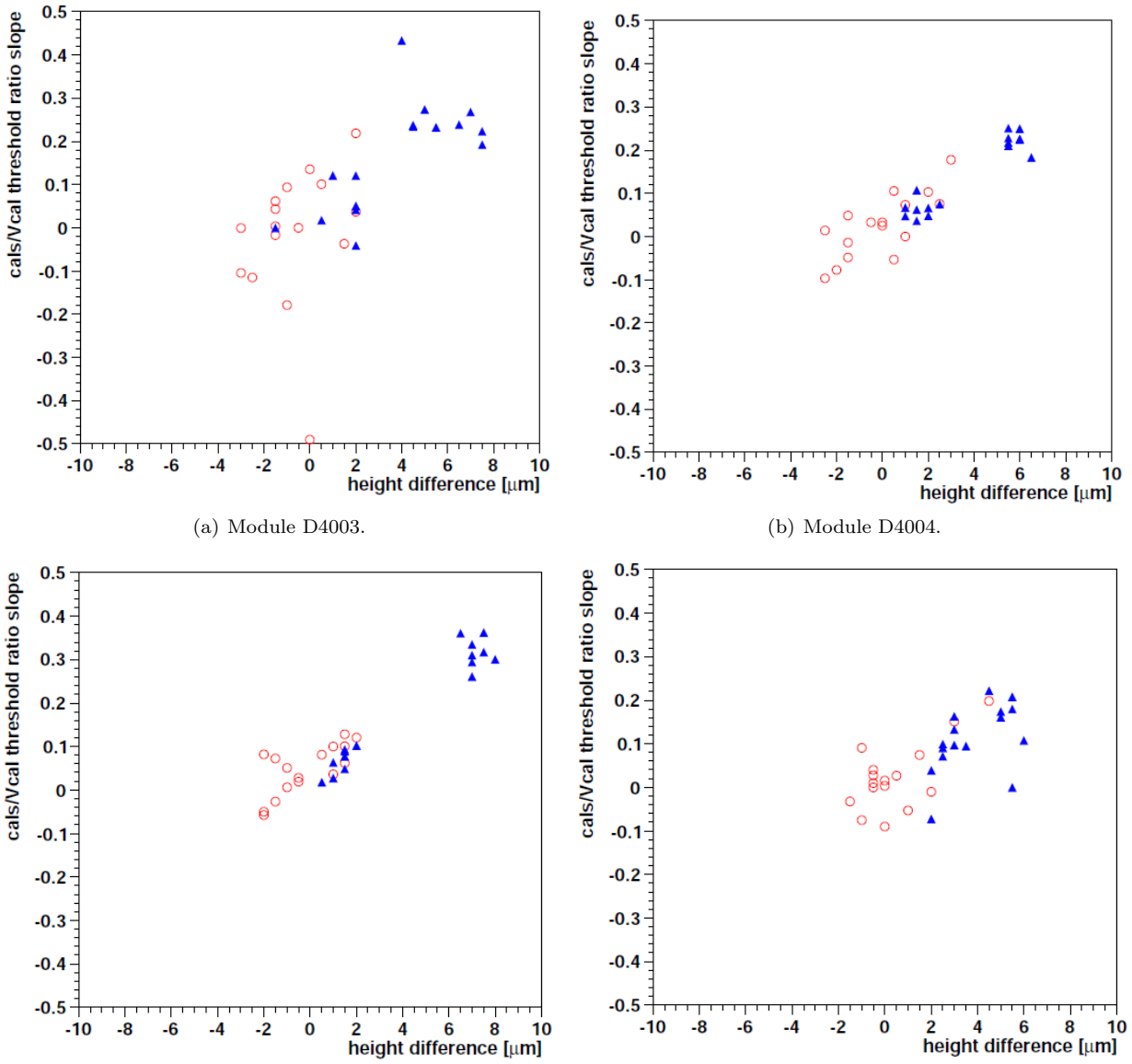

(a) Module D4003.

(b) Module D4004.

(c) Module D4005.

(d) Module D4006.

Figure 6: The gradient of the threshold ratio against the directly measured height variations. Analogous to aerodynamics, red circles indicate roll about an axis parallel to the columns, blue triangles indicate pitch about an axis parallel to the rows. The roll and pitch of each ROC is plotted. (Hopefully, the ROCs exhibit no yaw.)

Although far stronger on two of the modules, all four of them exhibits a generally positive correlation between the gradient obtained from the projections and the direct height measurements. A threshold ratio gradient of 0.25 seems to consistently correspond with a height variation of 6 μm.

3.2 Threshold Width Ratio Maps

Maps of the threshold width ratio for the same ROCs as in Figure 4 are shown in Figure 7.

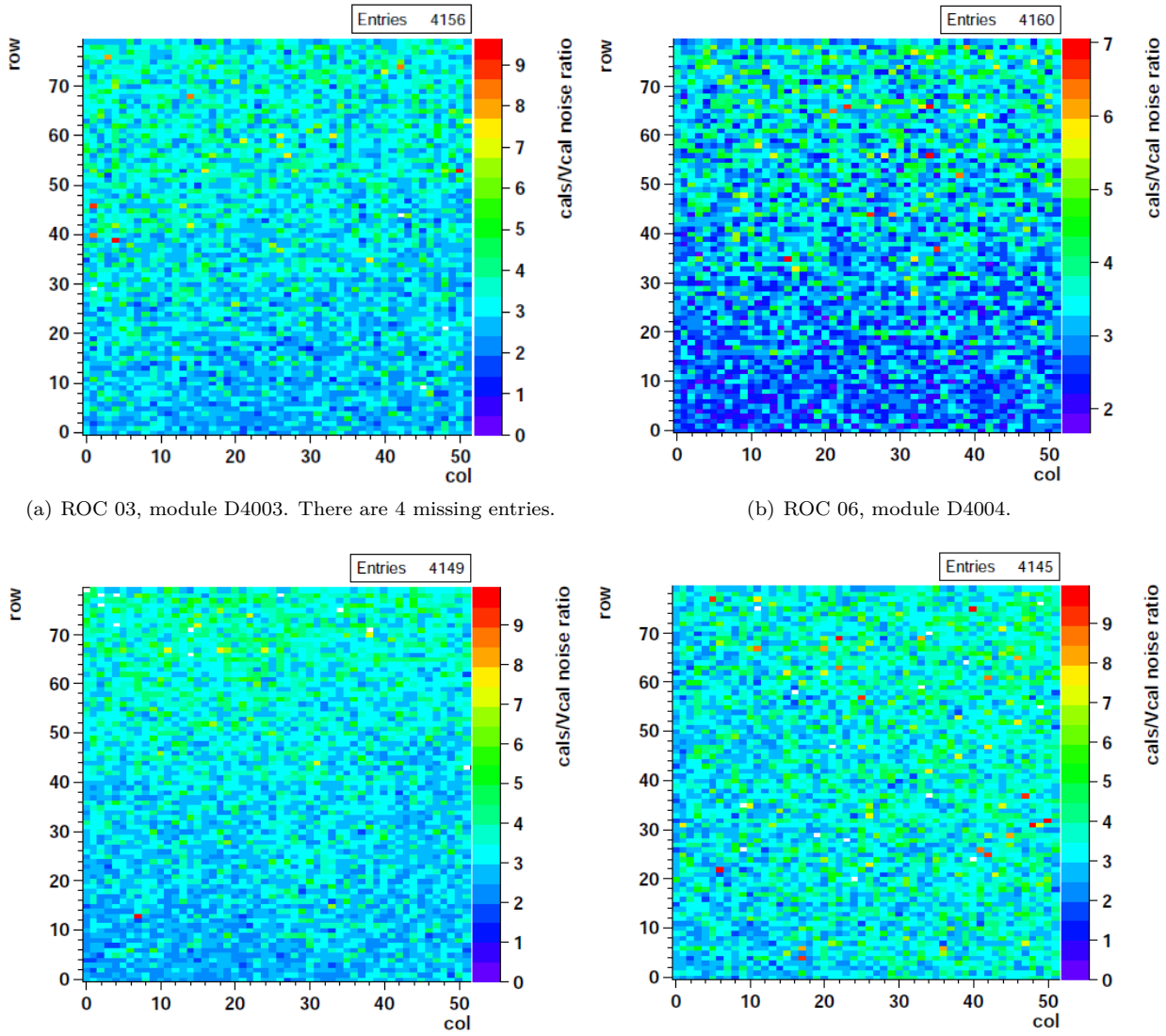

(a) ROC 03, module D4003. There are 4 missing entries.

(b) ROC 06, module D4004.

(c) ROC 07, module D4005. There are 11 missing entries.

(d) ROC 15, module D4006. There are 15 missing entries.

Figure 7: A threshold width ratio map of the same ROCs as before. Higher threshold width ratio should indicate a taller bump-bond.

Any possible trends on these maps are slightly more difficult to see. It is also interesting to note that the previously mentioned even/odd effect has been completely washed out. By taking column and row projections as before, the trends become more easily visible; these are shown in Figure 8. Again, the trends in the row direction are stronger than those in the column direction, and the row trends are consistent with the roof structure. The even/odd effect may be observable in Figure 8(a), but for the rest of them, the measurement seems dominated by statistical fluctuations. The gradients of these projections for each module are plotted against the direct measurements in Figure 9.

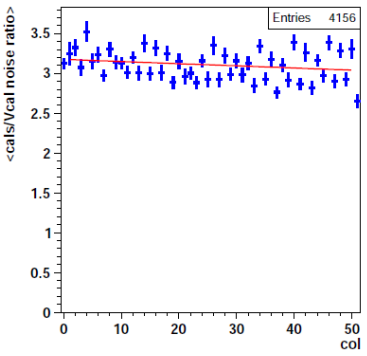

(a) ROC 03, module D4003 columns.

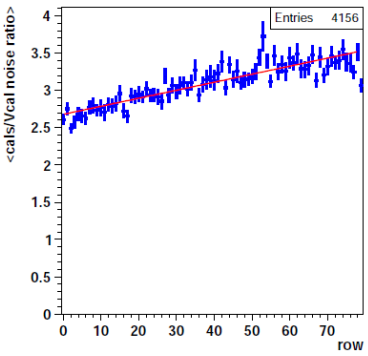

(b) ROC 03, module D4003 rows.

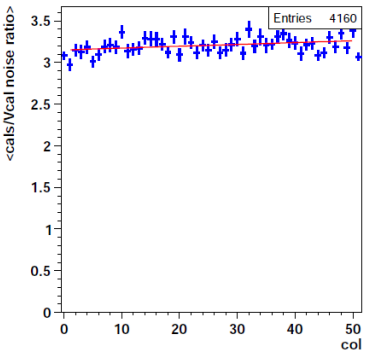

(c) ROC 06, module D4004 columns.

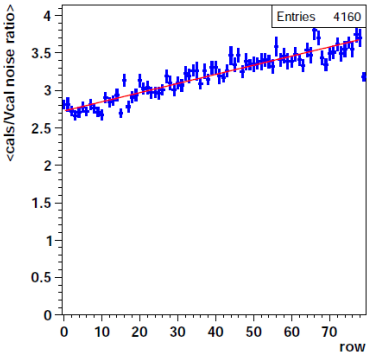

(d) ROC 06, module D4004 rows.

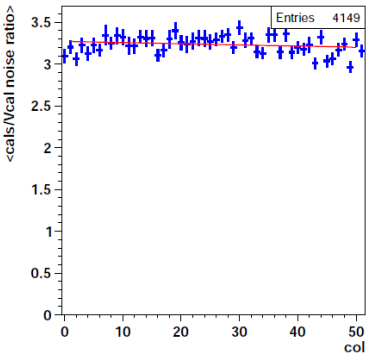

(e) ROC 07, module D4005 columns.

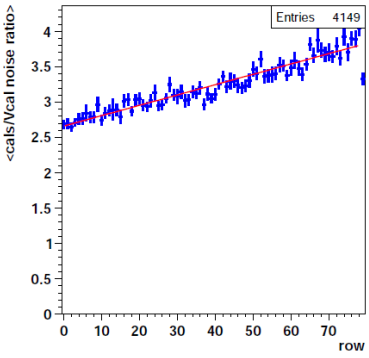

(f) ROC 07, module D4005 rows.

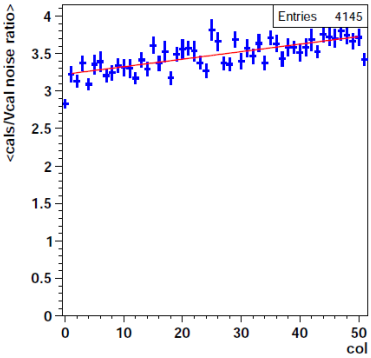

(g) ROC 15, module D4006 columns.

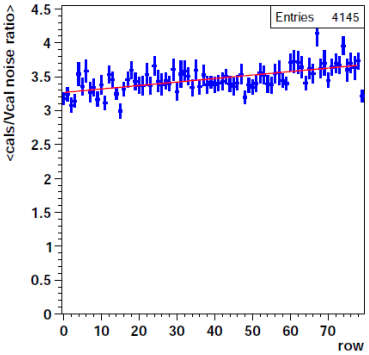

(h) ROC 15, module D4006 rows.

Figure 8: Column and row threshold width ratio projections from the threshold width ratio maps.

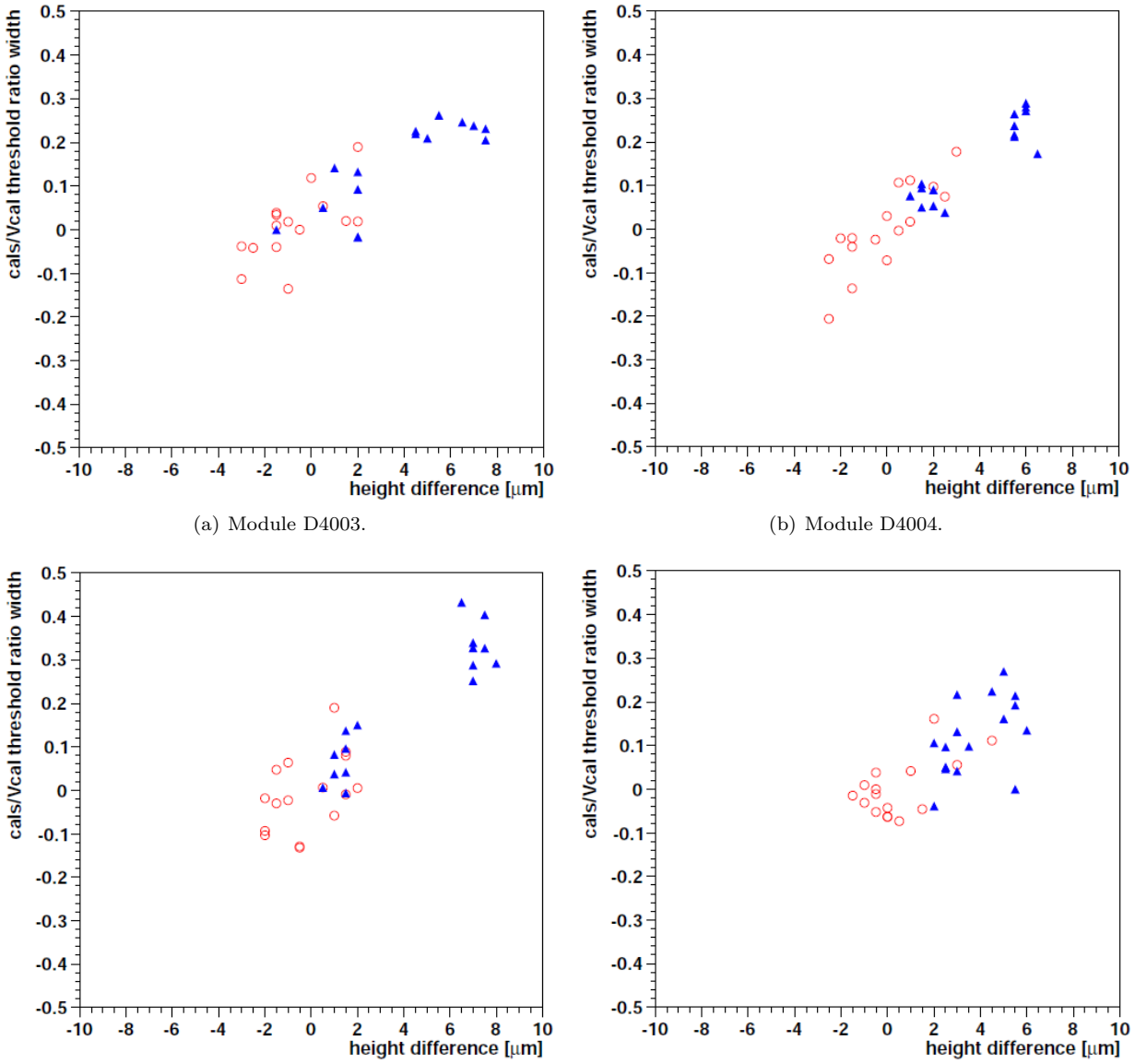

(a) Module D4003.

(b) Module D4004.

(c) Module D4005.

(d) Module D4006.

Figure 9: The gradient of the threshold width ratio against the directly measured height variations. Red circles indicate roll, blue triangles indicate pitch. The roll and pitch of each ROC is plotted.

The correlation of the threshold width ratio gradients to the height is similar to that of that of the threshold ratio gradients, and once again, a gradient of 0.25 indicates a height variation of 6 μm.

3.3 Threshold Ratio versus Width Ratio

The good agreement between the threshold ratio and threshold width ratio methods can be attributed to the good positive correlation between the two, as indicated in Figure 10. A threshold gradient of 0.25 corresponds to a threshold width gradient of 0.25, hence 6 μm corresponds to 0.25 for both of the gradients.

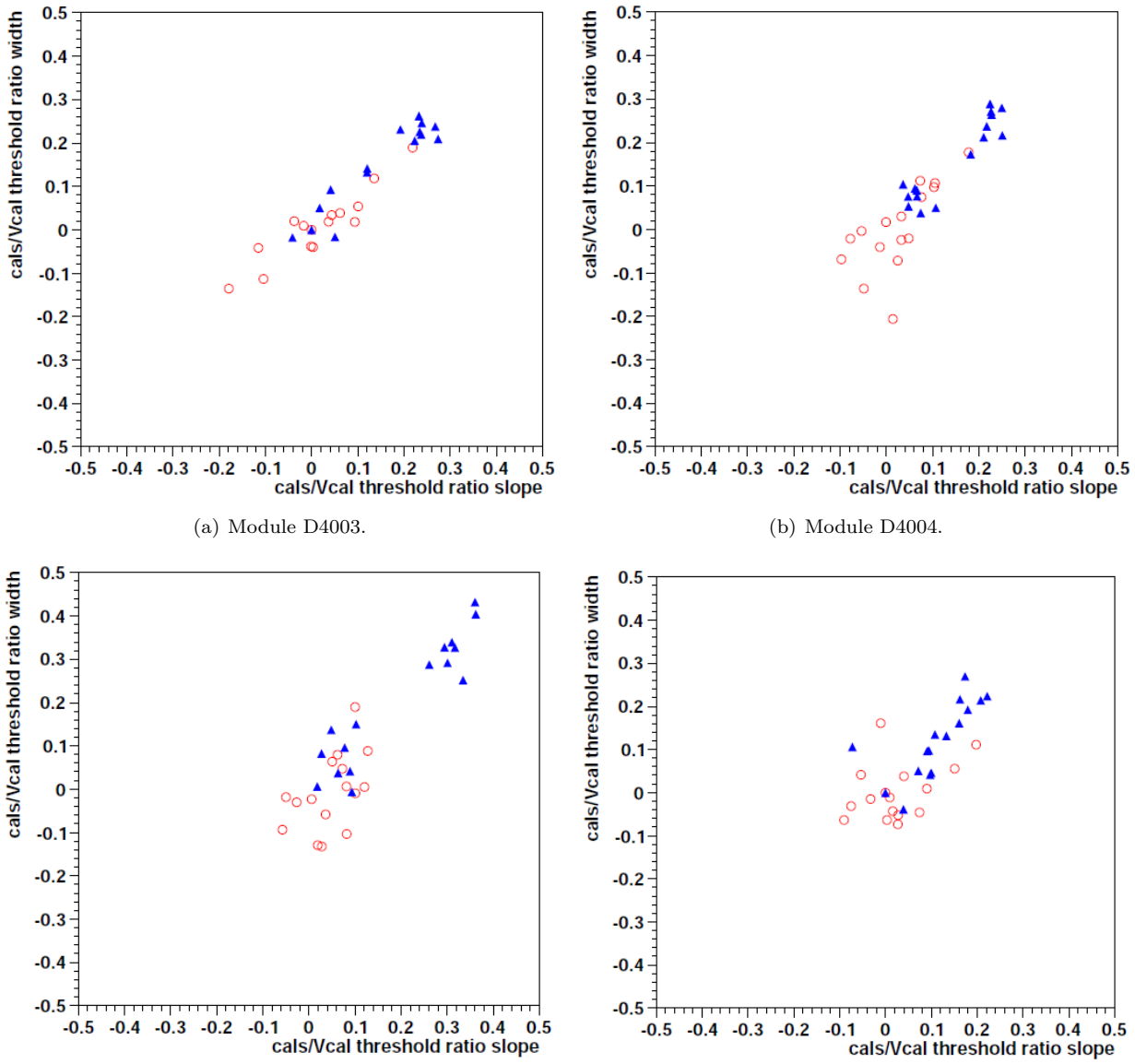

(a) Module D4003.

(b) Module D4004.

(c) Module D4005.

(d) Module D4006.

Figure 10: The gradient of the threshold width ratio against the gradient of the threshold ratio.

4 Conclusion

The correlation between the gradients from the threshold ratio and threshold width ratio method shows that the two methods are consistent with each other. The good correlation between both gradients and the direct height measurements shows that these methods provide a reasonable estimate of the height variation over the ROCs, added to the fact that they are a far simpler alternative than time consuming manual or destructive measurements, this demonstrates the viability of using these methods as a quality control check for modules produced in-house at DESY. A ratio gradient of 0.25 using both methods corresponds to a height variation of approximately 6 μm. Since these measurements were conducted, four additional modules have been constructed and in the near future these could also be directly measured and the results used to further validate the use of these methods.

References

[1] http://home.web.cern.ch/about/experiments/cms

[2] http://en.wikipedia.org/wiki/Compact_Muon_Solenoid

[3] http://hilumilhc.web.cern.ch/HiLumiLHC/index.html

[4] https://cds.cern.ch/record/1481838?ln=en